Volume 1 | Number 1 | Jan 2013 | Pages 1–100

Journal of
Materials Chemistry A

Materials for energy and sustainability
www.rsc.org/materialsA

ROYAL SOCIETY
OF CHEMISTRY

ROYAL SOCIETY
OF CHEMISTRY

www.rsc.org/materialsA

Journal Name

ARTICLE

An efficient near infrared photocatalyst of $Er^{3+}/Tm^{3+}/Yb^{3+}$ tridoped $(CaWO_4@(TiO_2/CaF_2))$ with multi-stage CaF_2 nanocrystal formation

Shouqiang Huang, Ziyang Lou, Aidang Shan, Nanwen Zhu,* Kaili Feng and Haiping Yuan

The formation process of CaF_2 is critical for the improvement of upconversion properties on the CaF_2 based upconversion photocatalysts, and a near-infrared (NIR) photocatalyst of $Er^{3+}/Tm^{3+}/Yb^{3+}$ tridoped $(CaWO_4@(TiO_2/CaF_2)$ (ETY-CTC) was synthesized. CaF_2 nanocrystals are multi-stage converted from $CaWO_4$ precursors, and the remaining $CaWO_4$ microspheres are self-wrapped by CaF_2 and TiO_2 nanocrystals to form the heterostructure photocatalyst. CaF_2 is found to connect with TiO_2 nanocrystals, instead of being coated by TiO_2, resulting in higher upconversion luminescence efficiency of ETY-CTC than that of pure $Er^{3+}/Tm^{3+}/Yb^{3+}$ tridoped $(CaWO_4@CaF_2)$. ETY-CTC possesses higher photocatalytic activities compared to $Er^{3+}/Tm^{3+}/Yb^{3+}$ tridoped $(CaWO_4@TiO_2)$ under NIR and UV-vis-NIR light irradiations, since more ·OH and $O_2^{·-}$ radicals, and higher electron-hole separation efficiency are obtained in the ETY-CTC system. The multi-stage formation of luminescence agents can be an attractive method for the synthesis of NIR photocatalysts with enhanced upconversion properties and photocatalytic activities.

Introduction

Full-spectrum utilization of solar energy in near-infrared (NIR) photocatalysts with the aid of upconversion agents has attracted enormous attention due to their promising application in water purification and solar cells.[1] The NIR driven photocatalytic activities of upconversion photocatalysts are mainly depended on the upconversion emission efficiencies of the luminescence agents, where fluorides with low phonon energies are commonly used as the host materials for lanthanide ions.[2] CaF_2 is a promising cost-effective upconversion luminescence agent for the improvement of photocatalytic activities in the NIR photocatalysts,[3] while unfavorable large-size particles of CaF_2 are obtained immediately, when $Ca(NO_3)_2$ is used as the calcium source in traditional methods during the fabrication of lanthanide ions (Yb^{3+}, Er^{3+} or Tm^{3+}) doped CaF_2.[3,4] Furthermore, the upconversion emission intensities of the core-shell NIR photocatalysts, such as Er^{3+}/Yb^{3+}-$(CaF_2@TiO_2)$,[3a] NaYF₄: Yb, Tm/TiO₂,[5] NaYF₄: Yb, Tm/ZnO,[6] NaYF₄: Yb, Tm/CdS,[7] and YF₃: Yb, Tm/TiO₂,[8] were decreased compared to those of pure fluoride agents, owing to the weakened excitation light penetration caused by the semiconductor shells. The lower upconversion efficiencies in NaYF₄: Yb, Er@SiO₂@TiO₂[9,10] were also observed, compared to their bare upconversion phosphors, which limit the development of the solar cells with high conversion efficiencies. To solve the issues above, slow formation of the upconversion luminescence agents might be one of the credible alternatives to control the particle size, and

the light penetration efficiency in the NIR photocatalyst system can also be improved with the multi-stage formation process, such as self-formed upconversion luminescence agents before and after the semiconductor coatings obtained. To find a new Ca-contained precursor is the pre-requirement for the high efficient CaF_2 based NIR photocatalyst formation.

$CaWO_4$ is widely used in phosphors,[11] microwave dielectrics,[12] and scintillators,[13] owing to its high density and stable physicochemical properties compared to other oxide materials.[11b] The W^{6+} ions with large electric charge and small radius in $CaWO_4$ can also decrease symmetries by their strong polarization.[14] Thus, $CaWO_4$ is a good oxide host material for lanthanide ions with high upconversion efficiency.[15] Importantly, the low solubility product of $CaWO_4$ ($K_{sp} = 8.7 \times 10^{-9}$) will control the release rate of Ca^{2+} ions,[16] which provides an opportunity to place CaF_2 ($K_{sp} = 2.7 \times 10^{-11}$) nanocrystals in-situ on the $CaWO_4$ microsphere surfaces ($CaWO_4/CaF_2$) continuously. The formation of lanthanide ions doped $CaWO_4/CaF_2$ will fulfill the requirements of high stability and excellent upconversion properties. Meanwhile, $CaWO_4$ is a wide-bandgap semiconductor, and its coupling with TiO_2 is beneficial for the charge carrier separation due to the formed heterojunction,[17] which will enhance the photocatalytic performances for the lanthanide ions doped $CaWO_4/CaF_2/TiO_2$ systems.

In this work, a novel NIR photocatalyst of $Er^{3+}/Tm^{3+}/Yb^{3+}$ tridoped $(CaWO_4@(TiO_2/CaF_2))$ (ETY-CTC) was synthesized via a hydrothermal method, and $Er^{3+}/Tm^{3+}/Yb^{3+}$ tridoped
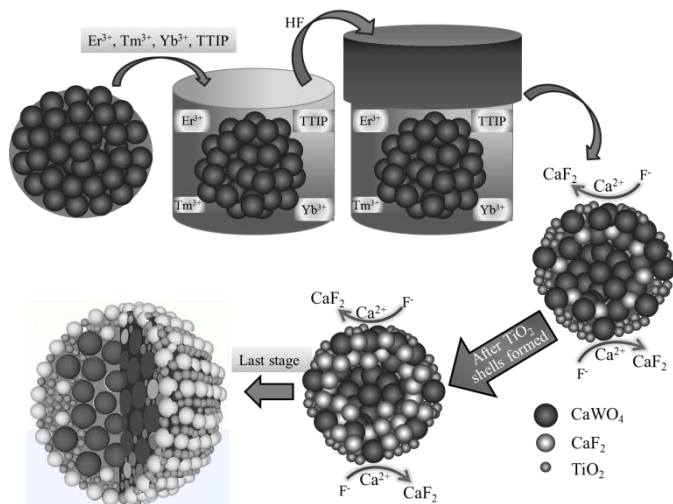
Fig. 1 Schematic illustration for the multi-stage fabrication of ETY-CTC.

$CaWO_4$ (ETY-C), $Er^{3+}/Tm^{3+}/Yb^{3+}$ tridoped ($CaWO_4@TiO_2$) (ETY-CT), $Er^{3+}/Tm^{3+}/Yb^{3+}$ tridoped ($CaWO_4@CaF_2$) (ETY-CC), and ETY-CC@TiO_2 (ETY-CC@T) were also fabricated simultaneously to compare their upconversion properties. The structures and morphologies of these samples were investigated, and their photocatalytic activities on the degradation of methyl orange (MO) under NIR and Ultraviolet-visible-Near Infrared (UV-vis-NIR) irradiations were tested as well.

Experimental Section

Chemicals and materials

$Ca(NO_3)_2 \cdot 4H_2O$, $Na_2WO_4 \cdot 2H_2O$, $Er(NO_3)_3 \cdot 5H_2O$, $Tm(NO_3)_3 \cdot 5H_2O$, $Yb(NO_3)_3 \cdot 5H_2O$, and titanium isopropoxide (TTIP, 98%) were all purchased from Sinopharm chemical Reagent Co. Ltd (China) with analytical grade and used as received.

Preparation of $CaWO_4$ microspheres

5 mmol $Na_2WO_4 \cdot 2H_2O$ was dissolved into 25 mL distilled water. Then 25 mL $Ca(NO_3)_2$ aqueous solution (0.2 M) was added drop by drop into the Na_2WO_4 solution under continuous stirring for 30 min. The resulting mixture was maintained at room temperature for 1 h. The products were obtained by centrifugation, washed with distilled water and absolute ethanol, and then dried at 60 ℃ for 12 h.

Preparation of ETY-CTC samples

In a typical synthesis, 2 mmol TTIP was dissolved in 20 mL absolute ethanol. $CaWO_4$, $Er(NO_3)_3 \cdot 5H_2O$, $Tm(NO_3)_3 \cdot 5H_2O$, and $Yb(NO_3)_3 \cdot 5H_2O$ (molar ratio of Ti^{4+}: Ca^{2+}: Yb^{3+}: Er^{3+}: Tm^{3+} is 1: 0.3: 0.2: 0.02: 0.02) were added into 40 mL distilled water and totally dispersed by ultrasonication. The pH of the mixture was adjusted to 1 by adding nitric acid, and followed by the slow addition of TTIP solution. The obtained mixture was stirring for 30 min, and 0.1 mL of HF (40%) was introduced and continuous stirring for 30 min. Then, the mixture was transferred into a 150 mL Teflon-lined stainless steel autoclave, and heated at 180 ℃ for 12 h (Fig. 1). The precipitates collected were dried at 60℃ for 12 h after separation and washing. The obtained powders were heated at 500 ℃ for 4 h to form ETY-CTC samples. For comparison
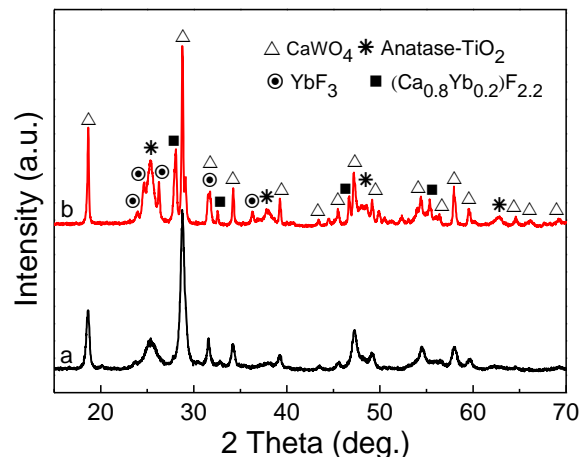
Fig. 2 XRD patterns of (a) ETY-CT and (b) ETY-CTC.

purposes, ETY-CC, ETY-CT, ETY-C, ETY-CC@T, and ETYN@T were also synthesized following the same procedure mentioned above.

Characterization

The crystal structures of the samples were identified by X-ray diffraction (XRD) on a Bruker D8 Advance X-ray Diffractometer at 40 kV and 40 mA using Cu K_α radiation (λ=1.5406 Å), and the crystal sizes were determined through the Scherrer formula.[3a] The morphologies were investigated by NoVa NanoSEM 230 field emission scanning electron microscope (FESEM) equipped with the AZTec X-Max80 energy-dispersive spectroscopy (EDS) instrument, and the JEM-2100F transmission electron microscope (TEM) instrument. The Brunauer-Emmett-Teller (BET) specific surface areas of the samples were determined from a nitrogen adsorption apparatus (Micromeritics, ASAP 2010 M + C) by N_2 adsorption at 77 K. The surface analysis was studied by the X-ray photoelectron spectroscopy (XPS, Kratos Axis Ultra[DLD]), and all the binding energies were calibrated with the C 1s peak at 284.8 eV. The absorption spectra were performed on the Lambda 750 UV-vis-NIR spectrophotometer, and the band gap energy was calculated referring to Tauc's formula.[3] Room temperature upconversion fluorescence spectra and the photoluminescence (PL) spectra were measured by a Hitachi F-7000 fluorescence spectrophotometer equipped with a 980 nm semiconductor solid laser with tunable power (Table S3). The electron spin resonance (ESR) spectra were recorded at room temperature with an EMX-8 ESR spectrometer (Bruker BioSpin Corp.).

Photocatalytic activities

The photocatalytic activities of the samples were evaluated by the decomposition of MO under 980 nm light and the NIR light ($\lambda \geq 780$ nm) irradiations (provided by 1000 W high pressure mercury lamp with a filter). 20 mg of the samples were added in the MO aqueous solutions (20 mg L^{-1}, 20mL). Before irradiation, the mixtures were kept in the dark with magnetically stirring for 2 h to establish an adsorption/desorption equilibrium. Every 30 min intervals, 2.0 mL of the mixtures were collected and centrifuged. The changed absorption peak intensities at 464 nm were detected by UV-vis spectrometer (Hitachi U-3900). Three dimension excitation-emission matrix (EEM) spectra measurements were conducted using Hitachi F-7000 fluorescence
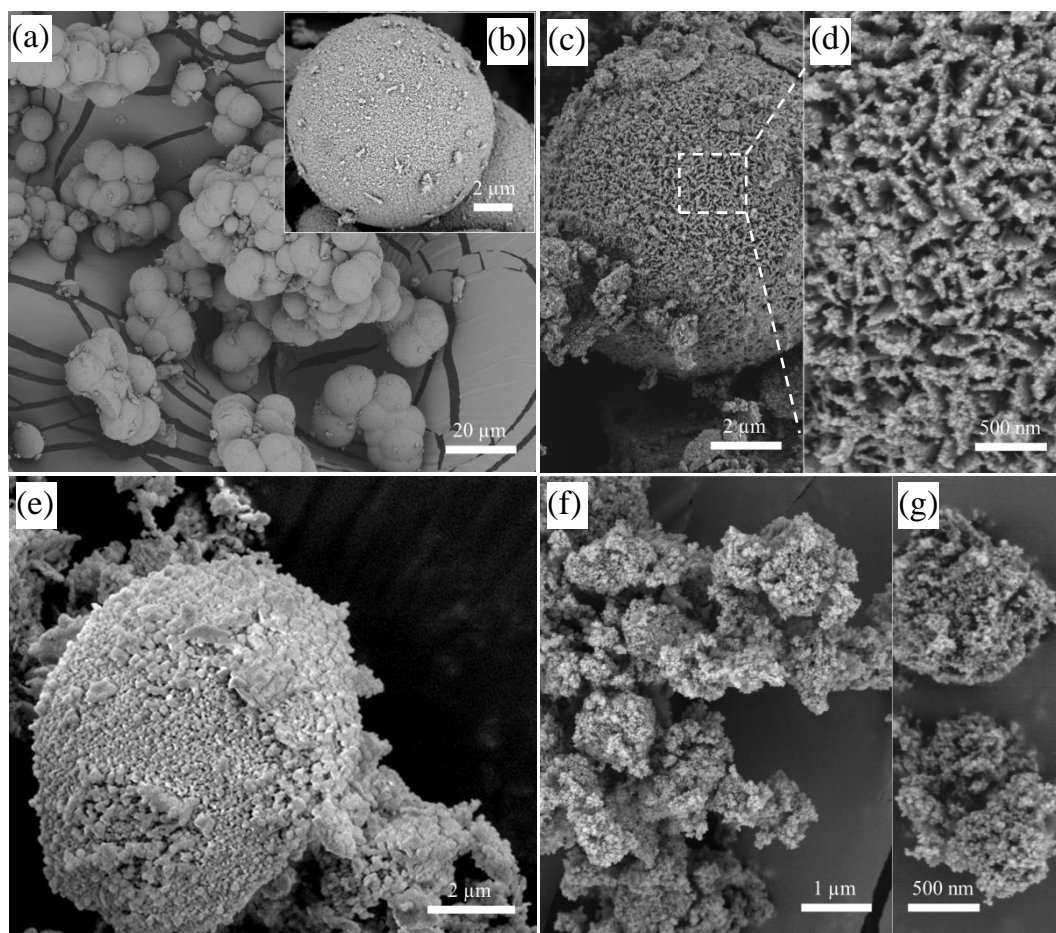
Fig. 3 SEM images of (a, b) pure CaWO$_4$, (c, d) ETY-CT, (e) ETY-CC, (f, g) ETY-CTC.

spectrophotometer. Emission scans were preformed from 250 to 500 nm at 10 nm steps, with excitation wavelengths from 200 to 350 nm at 10 nm widths. Meanwhile, the photoactivity tests of ·OH and O$_2$·$^-$ radicals were similar to the method mentioned for photodegradation of MO. Terephthalic acid (TA, 4×10^{-4} M in a 2×10^{-3} M NaOH solution) and Nitroblue tetrazolium (NBT, 1×10^{-3} M) solutions were used to determine the amounts of ·OH and O$_2$·$^-$ radicals generated from the samples, respectively.[3b,18]

Results and discussion

Characterization of the samples

Fig. 2 shows the XRD patterns of ETY-CT and ETY-CTC. For ETY-CT, besides the detected broad diffraction peak of anatase TiO$_2$ (PDF-#84-1285) at 25.26°, the main diffraction peaks are assigned to CaWO$_4$ (PDF-#72-1624). The crystal phases of ETY-CTC consist of CaWO$_4$, anatase TiO$_2$, (Ca$_{0.8}$Yb$_{0.2}$)F$_{2.2}$ (PDF-#87-0976), and YbF$_3$ (PDF-#74-2178). (Ca$_{0.8}$Yb$_{0.2}$)F$_{2.2}$ is a complex system contained two components of CaF$_2$ and YbF$_3$, since the Yb^{3+} ions take the Ca^{2+} lattice positions in CaF$_2$.[3] YbF$_3$ is bound to form immediately once the HF is added into the precursor solution (Fig. 1), owing that large amount of dissociative Yb^{3+} ions are presented, while the Ca^{2+} ions have to be released slowly from CaWO$_4$. Although there are sufficient F$^-$ ions in the solution, the complete transformation of CaF$_2$ from CaWO$_4$ needs a long time, i. e., five days at room temperature.[16] Thus, parts of CaWO$_4$ are maintained in the final products, which contribute to the charge carrier separation due to the formed CaWO$_4$/TiO$_2$ heterostructure.

According to the Scherrer formula, the average crystal sizes of TiO$_2$, CaWO$_4$, YbF$_3$, and (Ca$_{0.8}$Yb$_{0.2}$)F$_{2.2}$ in ETY-CTC are calculated to be 12.35, 45.56, 38.05, and 28.02 nm (Table S2†), respectively, exhibiting no significant difference in comparison with those of ETY-CC (Fig. S1†) and ETY-CT. It is found that the obtained crystal size of (Ca$_{0.8}$Yb$_{0.2}$)F$_{2.2}$ is much smaller than those (90-150 nm) fabricated by the direct addition of Ca(NO$_3$)$_2$.[3,4] Thus, the (Ca$_{0.8}$Yb$_{0.2}$)F$_{2.2}$ nanocrystals are able to produce in-situ on CaWO$_4$ surfaces and the remaining CaWO$_4$ will be wrapped by CaF$_2$ to self-assemble the core-shell structure, and their synergistic effect might provide efficient upconversion emissions.

The morphologies and microstructures of the samples are examined by SEM (Fig. 3) and TEM (Fig. 4). The initial pure CaWO$_4$ shows the perfect solid microsphere morphology (Fig. 3a and b), which is built by many CaWO$_4$ nanocrystals (Fig. S3†). In the case of ETY-CT (Fig. 3c), the CaWO$_4$ microsphere structure is not being destroyed, and the three-dimensional sheet-like surfaces are coated with TiO$_2$ nanoparticles (Fig. 3d). From Fig. 4a, it can be observed the CaWO$_4$@TiO$_2$ core-shell structure, since the lattice fringe spacings of 0.35 and 0.48 nm meet the (101) planes of TiO$_2$ shell and the (101) planes of CaWO$_4$ core (Fig. 4b), respectively.

With the additive of HF, the surface layers of the CaWO$_4$
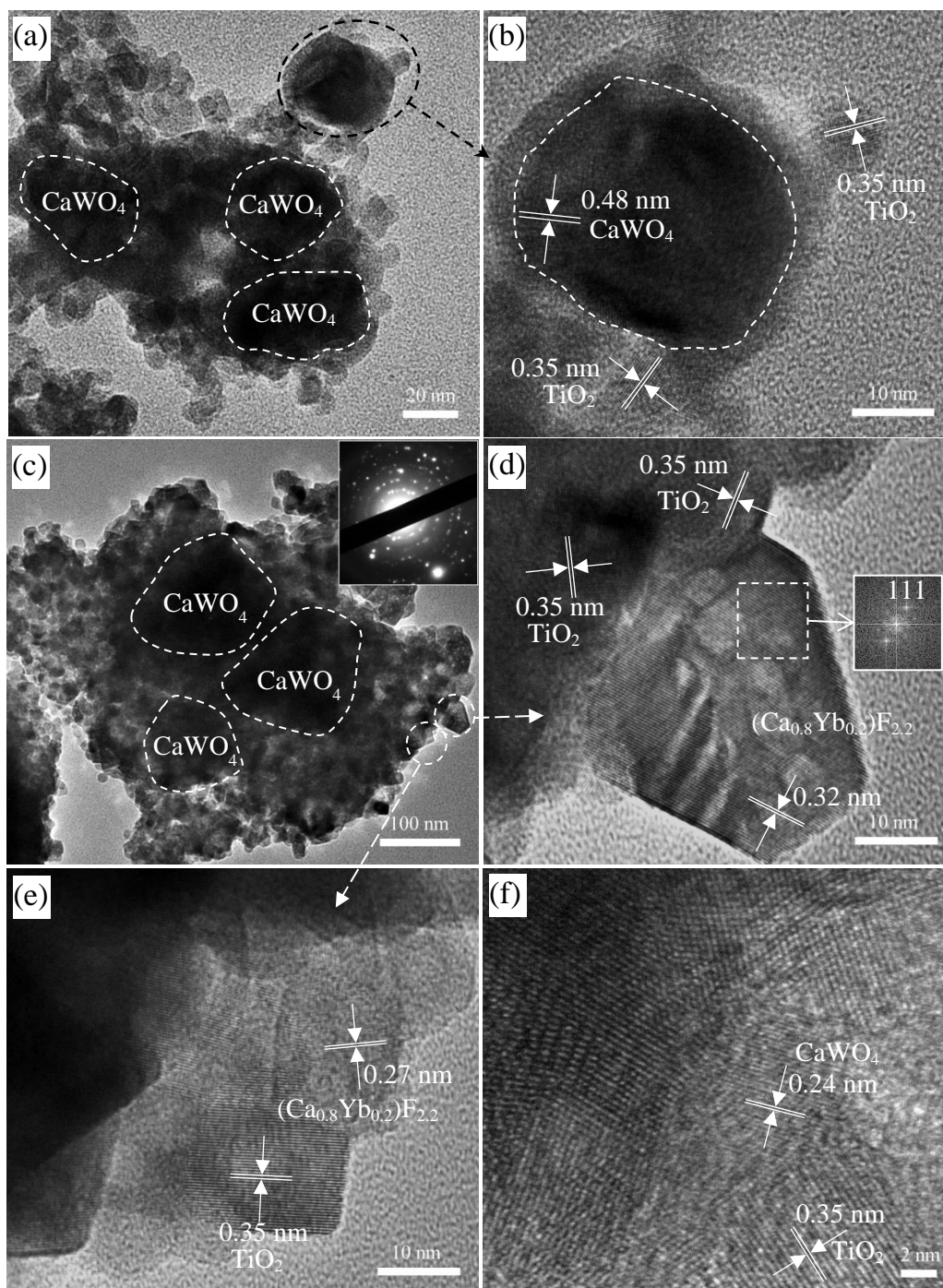
Fig. 4 (a) TEM and (b) HRTEM images of ETY-CT. (c) TEM (inset: selected-area electron diffraction pattern) and (d, e, f) HRTEM images (inset: Fourier transform electron diffraction pattern) of ETY-CTC.

microspheres are dissolved gradually, and substituted simultaneously by the in-situ formed CaF_2 layers, where ETY-CC is finally obtained (Fig. 3e and S4†). In the ETY-CTC system, most of the $CaWO_4$ microspheres have been etched seriously, resulting in various near-spherical aggregates coated by many nanoparticles with the property of porous (Fig. 3f, g and Table S1†). These aggregates consist of the $CaWO_4$ cores and the $TiO_2/(Ca_{0.8}Yb_{0.2})F_{2.2}$ coatings (Fig. 4c), and present the polycrystalline nature based on the selected-area electron diffraction pattern (top inset of Fig. 4c). A tooth-like

nanoparticle (~ 28 nm) is present in Fig. 4d with a lattice fringe spacing of 0.32, which is consistent with the (111) planes of $(Ca_{0.8}Yb_{0.2})F_{2.2}$, respectively, and the Fourier-transform electron diffraction pattern further confirms the particle is a single crystal. Meanwhile, a thin sheet-like crystal of $(Ca_{0.8}Yb_{0.2})F_{2.2}$ is also found in Fig. 4e, where the lattice fringe spacing of 0.27 nm is closed to its (200) planes. The crystal lattices at the bottom of the tooth-like $(Ca_{0.8}Yb_{0.2})F_{2.2}$ crystal belong to TiO_2 with (101) planes, as well as the TiO_2 nanosheet overlapped with the sheet-like
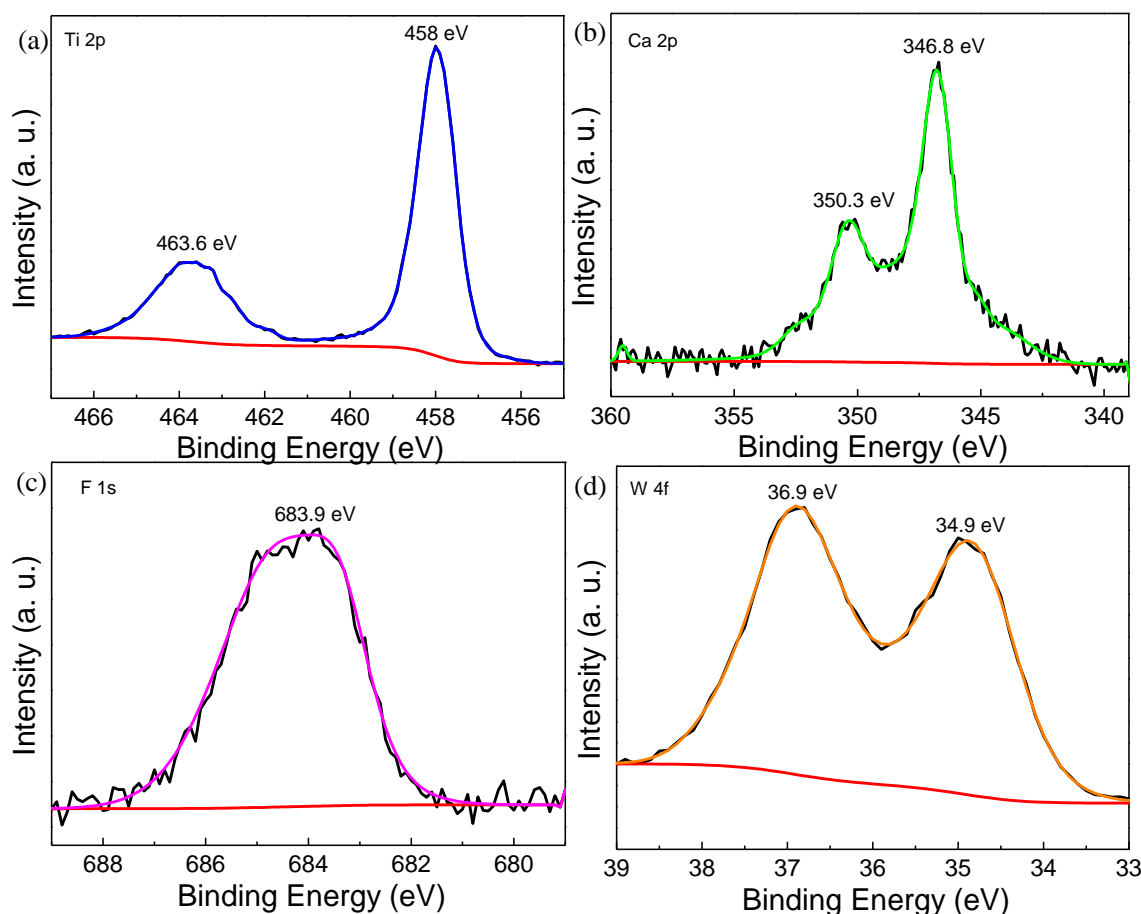
Fig. 5 XPS spectra of ETY-CTC: (a) Ti 2p, (b) Ca 1s, (c) F 1s, and (d) W 4f.

$(Ca_{0.8}Yb_{0.2})F_{2.2}$ crystal, meaning that the $(Ca_{0.8}Yb_{0.2})F_{2.2}$ nanocrystals are generated continuously after the TiO_2 coatings formed and thus present in the outmost surfaces. It is reasonable to suppose that the Ca^{2+} ions in $CaWO_4$ cores can diffuse through the porous TiO_2 coatings (Fig. 4c and Table S1†), and thus $(Ca_{0.8}Yb_{0.2})F_{2.2}$ generated can embed in the TiO_2 nanocrystals. These bared $(Ca_{0.8}Yb_{0.2})F_{2.2}$ nanocrystals will contribute to the high upconversion emission efficiency for ETY-CTC, since there is no TiO_2 layers weaken the light penetration to $(Ca_{0.8}Yb_{0.2})F_{2.2}$. Furthermore, the combined TiO_2 lattice and $CaWO_4$ lattice (Fig. 4f) can also facilitate the charge carrier transmission because of the well-defined heterostructure.

The element components in ETY-CT and ETY-CTC are measured by the EDS spectra and shown in Fig. S2a and b†, respectively. The Ti, Ca, Yb, Er, Tm, W, F, and O elements are found in ETY-CTC, and the atomic ratio of Ti: Ca: Yb: Er: Tm is 16.08: 3.88: 2.27: 0.17: 0.20 (Table S3†), which is close to its nominal atomic ratio of 1: 0.3: 0.2: 0.02: 0.02. As shown in Fig. S5a†, the survey-scan XPS spectra further demonstrate that the Ti, Ca, Yb, W, F, and O elements are present in ETY-CTC. Fig. 5a shows two peaks of Ti 2p at 458 and 463.6 eV, which meet the Ti $2p_{3/2}$ and Ti $2p_{1/2}$, respectively. The Ca 2p peaks at 346.8 and 350.3 eV correspond to Ca $2p_{2/3}$ and Ca $2p_{1/2}$ (Fig. 5b), respectively. The F 1s peak is detected at 683.9 eV (Fig. 5c), and the Yb 4d peaks at 185.7 and 199.5 eV are assigned to Yb $4d_{5/2}$ and Yb $4d_{3/2}$ (Fig. S5b†), respectively. The spin-orbit components of W $4f_{7/2}$ at 34.9 eV and W $4f_{5/2}$ at 36.9 eV are attributed to W atoms with 6+ oxidation state (Fig. 5d).[17b] The atomic concentration ratio of Ti: Ca: F: W: Yb is calculated to

be 33.41: 4.06: 5.43: 9.84: 2.57, according to the XPS results. Thus, TiO_2 is the predominant component in the outmost layers of ETY-CTC, combined with the present $(Ca_{0.8}Yb_{0.2})F_{2.2}$ and $CaWO_4$ nanocrystals, which will be helpful for the NIR light harvesting and the electron-hole pair separation.

Upconversion luminescence properties

The upconversion emission spectra of ETY-C, ETY-CC, ETY-CC@T, ETY-CT, and ETY-CTC upon 980 nm light excitation are recorded in Fig. 6. As the output currents increased from 1.0 to 3.0 A, the emission spectra profiles of ETY-CC (Fig. 6a and S6a†) and ETY-CTC (Fig. 6b and S6b†) are almost unchanged, while ETY-CTC possesses higher emission intensities in the visible light wavelength range (400-700 nm) compared to those of ETY-CC (Fig. 6c), and the UV light emissions (365 and 382 nm) of them almost stay at the same levels. Considering the band gap energy of 2.92 eV for ETY-CTC (Table S2† and Fig. S7†), it can be inferred that the UV light is absorbed stronger by TiO_2 compared to the violet light (410 nm). The upconversion luminescence peaks mainly include the red (659 nm), green (554 and 525 nm), violet (410 nm), and UV (382 nm) emissions, which are attributed to the $^4F_{9/2} \rightarrow ^4I_{15/2}$, $^2H_{11/2} \rightarrow ^4I_{15/2}$, $^4S_{3/2} \rightarrow ^4I_{15/2}$, $^2H_{9/2} \rightarrow ^4I_{15/2}$, and $^4G_{11/2} \rightarrow ^4I_{15/2}$ transitions of Er^{3+} ions, respectively (Fig. 6c). Meanwhile, the blue (477 nm) and UV (365 nm) emissions are corresponded to the $^1G_4 \rightarrow ^3H_6$ and $^1D_2 \rightarrow ^3H_6$ transitions of Tm^{3+} ions, respectively.

It should point out that ETY-CTC exhibits better
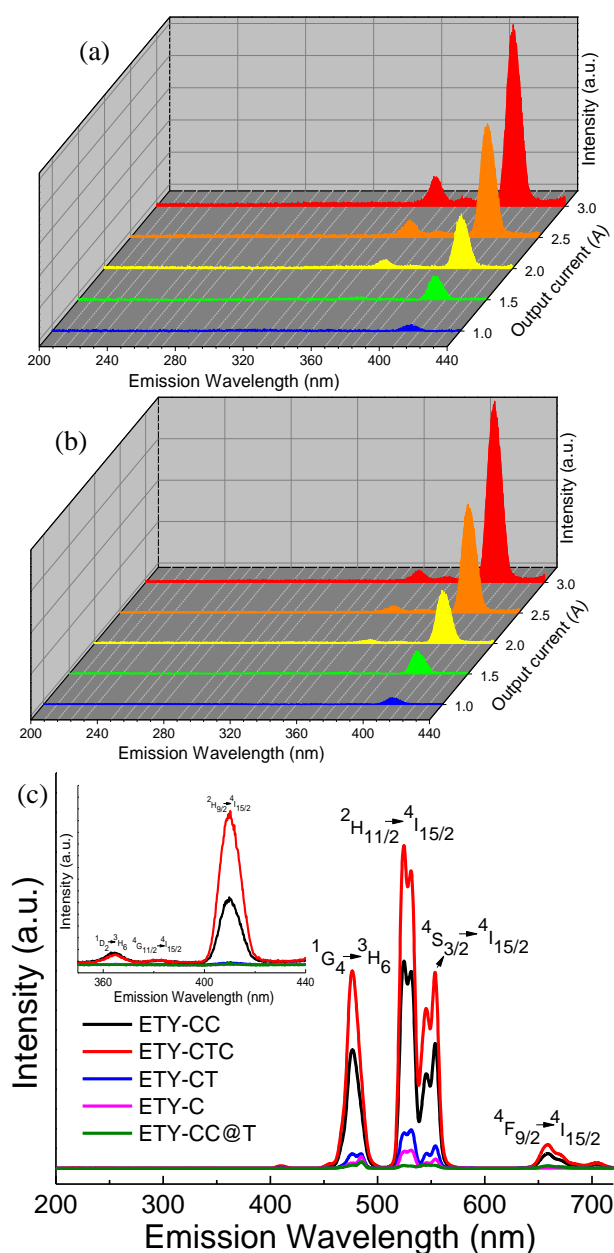
Fig. 6 Upconversion luminescence spectra of (a) ETY-CC and (b) ETY-CTC under 980 nm NIR excitation with different output currents (1.0-3.0 A). (c) Upconversion luminescence spectra of ETY-CC, ETY-CTC, ETY-CT, ETY-C, and ETY-CC@T under 980 nm NIR excitation (output current = 3.0 A).

upconversion property compared to those of ETY-CT, ETY-C, ETY-CC@T, and even the pure ETY-CC (Fig. 6c and S8†), except for the 365 and 382 nm UV light absorbed by TiO_2. Based on the previous reported NIR core-shell photocatalysts,[3a,5-10] all of their upconversion emission intensities are lower than those of pure luminescence agents, due to the barriers of the semiconductor shells and the weakened excitation light penetration. There are also some different cases, where the upconversion properties of NIR photocatalysts are not decreased in the emission wavelength of 250~700 nm besides the absorbed parts,[19] while in the longer wavelength, such as the 800 nm emission intensity of Tm^{3+} is still unknown. The main reason might be related to the surface
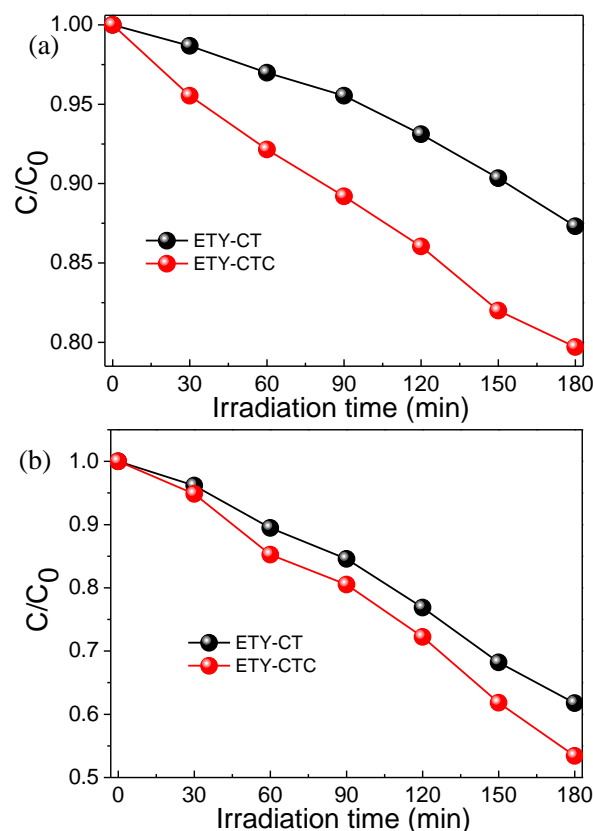
Fig. 7 C/C_0 conversion plots of MO for ETY-CT and ETY-CTC under (a) 980 nm (output current = 2.0 A) and (b) NIR light (≥ 780 nm) irradiations.

morphologies and the thickness of the semiconductor shells. Nevertheless, the semiconductor shells, such as TiO_2, ZnO, and CdS, are different from the CaF_2 or $NaYF_4$ passivation shells with excellent optical transparency to improve the upconversion emission intensities greatly.[20] With increasing the light scattering by the used semiconductor shells, the NIR light penetration to the upconversion luminescence agent cores will be often weakened more or less. To reduce the loss of excitation light penetration rate, a special structure is formed in the ETY-CTC system, where the $(Ca_{0.8}Yb_{0.2})F_{2.2}$ nanocrystals located at the outmost surfaces are not fully coated by TiO_2 (Fig. 4), resulting in sufficient exciting light harvesting to produce strong upconversion emission intensity. Taking the fabrication process of ETY-CC and ETY-CTC into account, the distribution of $Er^{3+}/Tm^{3+}/Yb^{3+}$ ions have been changed by the additional TiO_2 coatings. According to the surface compositions estimated from the XPS analysis (Table S3†), the atomic ratios of Ca: F: W: Yb are 1: 1.34: 2.42: 0.63 for ETY-CTC and 1: 1.65: 0.27: 0.25 for ETY-CC. The increase of Yb^{3+} content in the surface layer of ETY-CTC can absorb more 980 nm light energy,[20b,21] which will transfer more energy to Er^{3+} and Tm^{3+} ions to generate higher emission intensity compared to ETY-CC. The Er^{3+} and Tm^{3+} quench effect can also be reduced in the outmost layers of ETY-CTC, since they can be well-separated by the TiO_2 nanocrystals and the Yb^{3+} ions with high concentration.[4] Meanwhile, the surface quenching effect may be suppressed in ETY-CTC, due to the modulation through the TiO_2 coatings.[22] Other determined factors may be related to the suitable increased coating thickness and the changed morphologies.[23] On the other hand, owing to the multi-stage
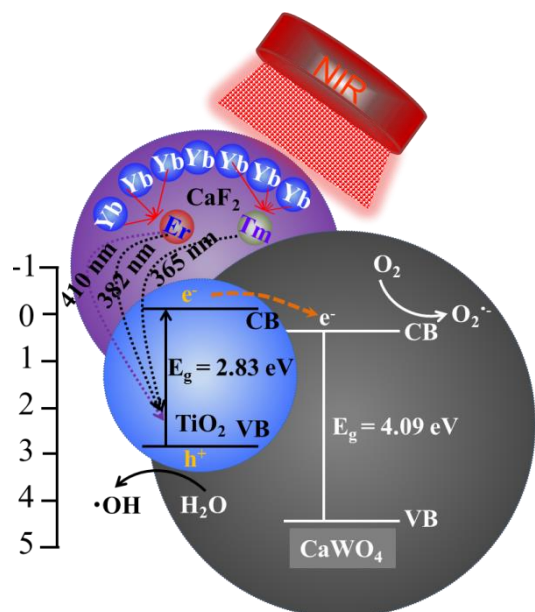
Fig. 8 Schematic electronic band structure and electron-hole pair separation of ETY-CTC under NIR light irradiation.

formed CaF_2 agents, the obtained NIR photocatalyst of ETY-CTC still possesses excellent upconversion property compared to ETY-CC, and it is the guarantee of high NIR light driven photocatalytic activities.

Photocatalytic activities

The photocatalytic activities of ETY-CT and ETY-CTC are tested and compared in MO decomposition experiments under 980 nm and NIR light ($\lambda \geq 780$ nm) irradiations. As shown in Fig. S9, the maximum absorbance of MO at 464 nm decreases steadily as the irradiation time increased to 180 min over ETY-CTC, and higher degradation rates of 20.29% and 46.57% are obtained using 980 nm and NIR light irradiations (Fig. 7), followed by ETY-CT with 12.69% and 38.23%, respectively. It can be seen from Fig. S10 that there is no MO degradation in the absence of photocatalysts, and neither of pure TiO_2 and $CaWO_4$ has photocatalytic activity under NIR light irradiation. In addition, ETY-CC@T also shows low degradation rates of 9.17% and 33.69% under 980 nm and NIR light driven conditions (Fig. S12), respectively, due to its large decreased upconversion emission intensity and the inert TiO_2 shells without active centers ($Er^{3+}/Tm^{3+}/Yb^{3+}$) compared to those of ETY-CTC.[3a]

In the ETY-CTC system, Yb^{3+} ions absorb the NIR light and transfer energy to Er^{3+} and Tm^{3+} ions to emit UV (365 and 382 nm) and violet (410 nm) light (Fig. 8), which enable to excite TiO_2 to produce oxidative valance band (VB) holes (h^+) and reductive conduction band (CB) electrons (e^-). To elucidate the heterostructure between $CaWO_4$ and TiO_2, the relative band edge positions of them are investigated through the following equation: $E_{CB} = X - E_0 - 0.5E_g$.[24] X is the absolute electronegativity of the semiconductors (for TiO_2, X = 5.81 eV;[25] for $CaWO_4$, X = 7.045 eV[17a]), E_0 is the energy of free electrons on the hydrogen scale (~ 4.5 eV), E_g is the band gap
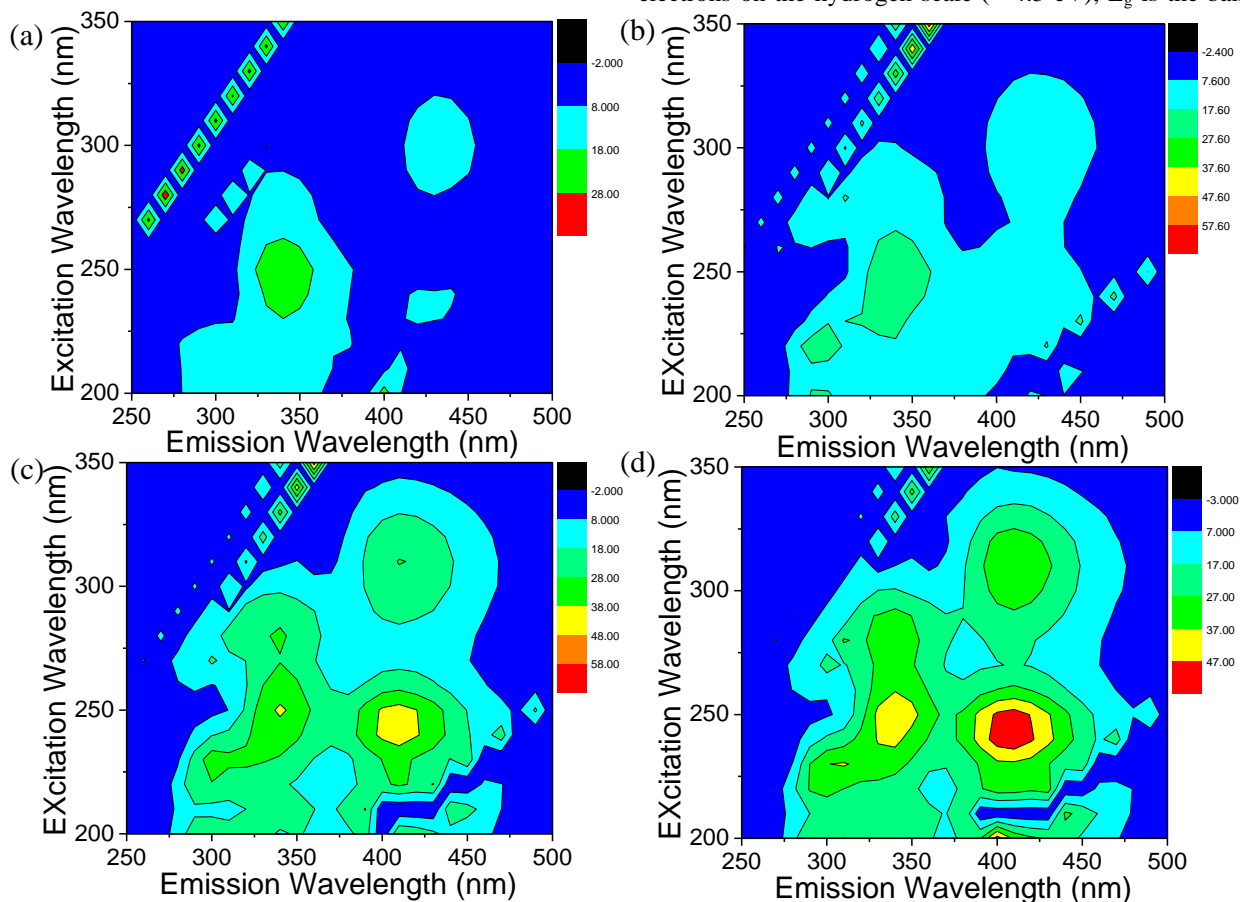
Fig. 9 EEM fluorescence spectra of MO for ETY-CTC under NIR light irradiation: (a) 0 min, (a) 30 min, (a) 120 min, and (a) 180 min.
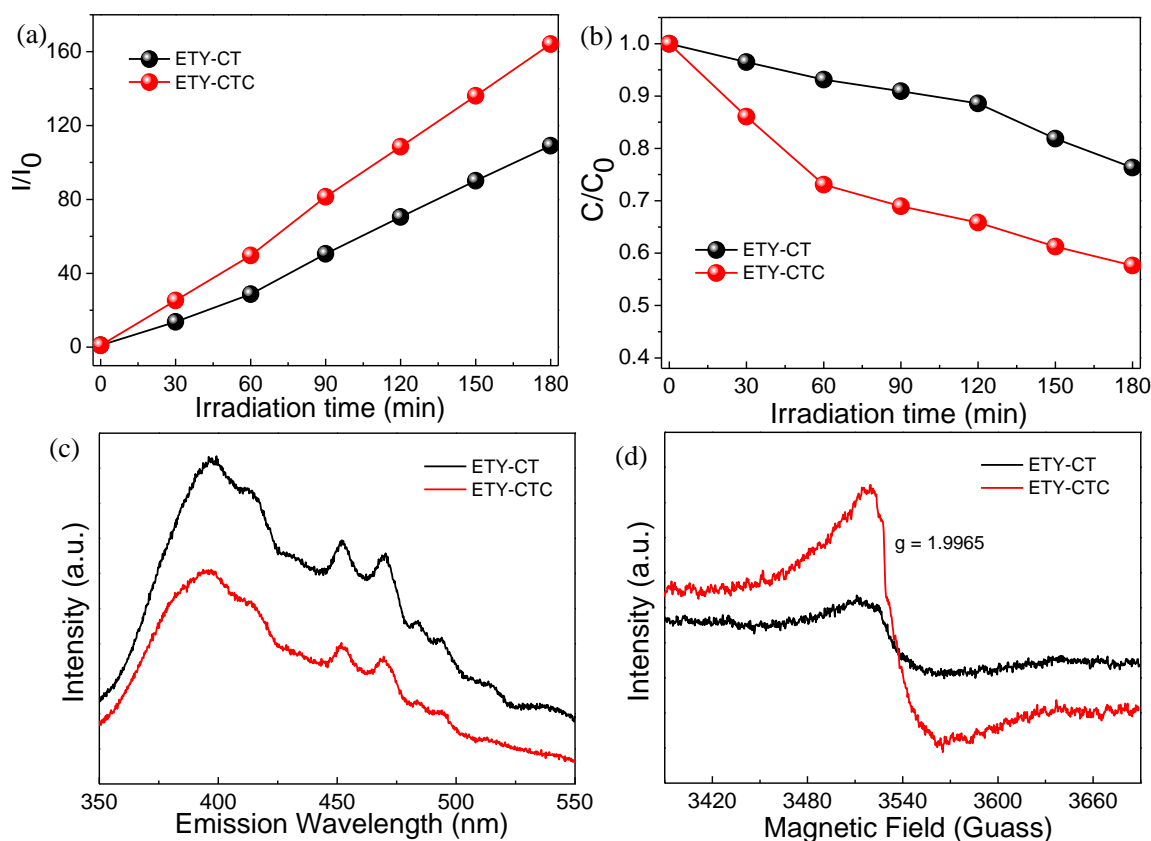
Fig. 10 Photocatalytic activities for (a) ·OH and (b) $O_2^{·-}$ production under 980 nm light irradiation (output current = 2.0 A). (c) PL emission spectra excited at 300 nm at room temperature and (d) ESR spectra for ETY-CT and ETY-CTC.

of the semiconductor (for TiO_2, E_g = 2.83 eV[3a]; for $CaWO_4$, E_g = 4.09 eV[17a]). The E_{CB} values of TiO_2 and $CaWO_4$ are calculated to be -0.105 and 0.5 eV, respectively, and the corresponding E_{VB} values are 2.725 and 4.59 eV for TiO_2 and $CaWO_4$, respectively. As shown in Fig. 8, the generated electron can transfer from the CB of TiO_2 to the lower CB edge of $CaWO_4$, and thus electron-hole pair separation is promoted. Then, the ·OH radicals can be generated through the reaction between holes and the surface adsorbed H_2O, and the electrons can be scavenged by the surface adsorbed O_2 to yield $O_2^{·-}$ radicals.[26] It can be found that both of ·OH and $O_2^{·-}$ radicals increase linearly as the irradiation time extended (Fig. 10a, b, S16† and S17†). ETY-CTC has stronger ability to produce both ·OH and $O_2^{·-}$ radicals, and a better decomposition performance is present compared to ETY-CT.

In the photocatalytic degradation process, the chromophoric azo group (–N=N–) of MO molecules can be attacked and destroyed by the ·OH and $O_2^{·-}$ radicals, producing aromatic intermediates and further forming various low molecular weight byproducts before mineralizing.[27] Fig. 9 shows the EEM spectra of MO over ETY-CTC with different NIR light irradiation time. Before irradiation, MO solution main contains one fluorescence peak at excitation/emission wavelengths Ex/Em = 220-250 nm/330-350 nm (Fig. 9a), which represents the aromatic-like compounds.[28] As the NIR light irradiation time extended, the peak intensity of aromatic-like compounds increased gradually (Fig. 9b-d), and two other fluorescence peaks display clearly at Ex/Em = 230-250/390-440 nm and 290-320/400-430. They may be attributed to the phototransformation intermediates, such as hydroxy derivatives.[28a] Based on the enhanced fluorescence peaks, it can

be inferred that decolorization is the predominant reaction, and mineralization of MO has not occurred yet during the used NIR light irradiation time (~ 180 min).

The photocatalytic activities are further evaluated under UV-vis-NIR irradiation (Fig. S11 and S12†). In the first irradiation of 30 min, the degradation rates in ETY-CTC, ETY-CT, and ETY-CC@T are 91.69%, 84.77%, and 58.71%, respectively, coherently with the NIR-driven photocatalytic results. Benefit from the incorporation of CaF_2, the PL emission intensity of ETY-CTC is lower than that of ETY-CT (Fig. 10c), indicating its better electron-hole separation ability, which is responsible for the higher photocatalytic activities compared to ETY-CT. The UV-vis-NIR driven EEM spectra of MO over ETY-CTC are shown in Fig. S14†, and they are very different from those obtained under NIR light irradiation. The complete decolorization and partial mineralization reactions have occurred in the initial irradiation of 30 min (Fig. S14b†), and the purity of the obtained solution after 180 min (Fig. S14d†) is close to the used distilled water in this study (Fig. S15†).

The broad PL spectra of the samples include several emission peaks. Accordingly, the 396 nm peak is emitted by $CaWO_4$,[11a] and the 412 nm peak is attributed to defect levels near the valence band of TiO_2.[29] The emission peaks at 452, 470, 484, and 494 nm are associated with the oxygen defects, representing the different types of charge (F, or F^+ centers) oxygen vacancy states.[30] Furthermore, the oxygen vacancies of the samples are characterized by ESR spectroscopy (Fig. 8d), and the symmetry ESR signal located at g = 1.9965 is assigned to oxygen vacancy, and no Ti^{3+} (g = 1.965, 1.938, and 1.916) or O_2^- (g = 2.02) signals can be measured.[31] With the addition of CaF_2, the ESR signals of ETY-CTC are stronger than that of

ETY-CT, and the increased oxygen vacancies can be considered as electron traps to enhance the electron-hole pair separations.[32] The oxygen vacancies can also react with the absorbed O_2 to generate bridging O_2 dimers,[33] which contribute the photocatalytic activity for the NIR photocatalysts.

Conclusions

In conclusion, a heterostructure NIR photocatalyst of ETY-CTC was synthesized, where CaF_2 nanocrystals are slowly fabricated from $CaWO_4$ precursors and embedded in $CaWO_4$ surfaces, and the remaining $CaWO_4$ microspheres are self-wrapped by CaF_2 and TiO_2 nanocrystals to form heterostructure. Benefits from this special structure, ETY-CTC exhibits better upconversion property compared to those of ETY-C, ETY-CT, ETY-CC@T, and even the pure ETY-CC luminescence agent. Under NIR and UV-vis-NIR light irradiations, ETY-CTC has higher MO degradation rates compared to ETY-CT, owing to the enhanced upconversion property, the increased electron-hole separation efficiency, and the enhanced oxygen vacancy signals in the ETY-CTC system.

Acknowledgements

Notes and references

School of Environmental Science and Engineering, Shanghai Jiao Tong University, 800 Dongchuan Road, Shanghai, 200240, P. R.China. Fax: +86 21 54743710; Tel: +86 21 54743710; E-mail: nwzhu@sjtu.edu.cn

† Electronic Supplementary Information (ESI) available: Additional mentioned tables and figures in the text. See DOI: 10.1039/b000000x/

1   (a) E. L. Cates, S. L. Chinnapongse, J. H. Kim and J. H. Kim, *Environ. Sci. Technol.*, 2012, **46**, 12316-12328; (b) X. Y. Huang, S. Y. Han, W. Huang and X. G. Liu, *Chem. Soc. Rev.*, 2013, **42**, 173-201.

2   (a) M. Haase and H. Schäfer, *Angew. Chem. Int. Ed.*, 2011, **50**, 5808–5829; (b) F. Wang and X. G. Liu, *Chem. Soc. Rev.*, 2009, **38**, 976-989.

3   (a) S. Q. Huang, L. Gu, C. Miao, Z. Y. Lou, N. W. Zhu and H. P. Yuan, A. D. Shan, *J. Mater. Chem. A*, 2013, **1**, 7874-7879; (b) S. Q. Huang, N. W. Zhu, Z. Y. Lou, L. Gu, C. Miao, H. P. Yuan and A. D. Shan, *Nanoscale*, 2014, **6**, 1362-1368.

4   C. Y. Cao, W. P. Qin, J. S. Zhang, Y. Wang, G. F. Wang, G. D. Wei, P. F. Zhu, L. L. Wang and L. Z. Jin, *Opt. Commun.*, 2008, **281**, 1716-1719.

5   D. X. Xu, Z. W. Lian, M. L. Fu, B. L Yuan, J. W. Shi and H. J. Cui, *Appl. Catal., B*, 2013, **142-143**, 377-386.

6   X. Y. Guo, W. Y. Song, C. F. Chen, W. H. Di and W. P. Qin, *Phys. Chem. Chem. Phys.*, 2013, **15**, 14681-14688.

7   C. H. Li, F. Wang, J. Zhua and J. C. Yu, *Appl. Catal., B*, 2010, **100**, 433-439.

8   (a) W. P. Qin, D. S. Zhang, D. Zhao, L. L. Wang and K. Z. Zheng, *Chem. Commun.*, 2010, **46**, 2304-2306; (b) Z. Q. Li, C. L. Li, Y. Y. Mei, L. M. Wang, G. H. Dua and Y. J. Xiong, *Nanoscale*, 2013, **5**, 3030-3036.

9   L. L. Liang, Y. M. Liu, C. H. Bu, K. Guo, W. W. Sun, N. Huang, T. Peng, B. Sebo, M. M. Pan, W. Liu, S. S. Guo and X. Z. Zhao, *Adv. Mater.*, 2013, **25**, 2174-2180.

10 L. L. Liang, Y. M. Liu and X. Z. Zhao, *Chem. Commun.*, 2013, **49**, 3958-3960.

11 (a) R. P. Jia, G. X. Zhang, Q. S. Wu and Y. P. Ding, *Appl. Phys. Lett.*, 2006, **89**, 043112; (b) Y. G. Su, L. P. Li and G. S. Li, *Chem. Mater.*, 2008, **20**, 6060-6067.

12 L. Cheng, P. Liu, S. X. Qu and H. W. Zhang, *J. Alloys Compd.*, 2013, **581**, 553-557.

13 A. Erb and J. C. Lanfranchi, *CrystEngComm*, 2013, **15**, 2301-2304.

14 Y. Huang, H. Seo, Y. Yang and J. Zhang, *Mater. Chem. Phys.*, 2005, **91**, 424-430.

15 J. H. Chung, J. -I. Lee, S. -L. Ryu and J. H. Ryu, *Ceram. Int.*, 2013, **39**, S369- S372.

16 W. S. Wang, L. Zhen, C. Y. Xu, J. Z. Chen and W. Z. Shao, *ACS Appl. Mater. Interfaces*, 2009, **1**, 780-788.

17 (a) Y. D. Guo, G. K. Zhang, H. H. Gan and Y. L. Zhang, *Dalton Trans.*, 2012, **41**, 12697-12703; (b) J. Tian, Y. Sang, G. Yu, H. Jiang, X. Mu and H. Liu, *Adv. Mater.*, 2013, **25**, 5075-5080.

18 (a) L. Q. Ye, J. Y. Liu, Z. Jiang, T. Y. Penga and L. Zan, *Nanoscale*, 2013, **5**, 9391-9396; (b) C. L. Yu, G. Li, S. Kumar, K. Yang and R. C. Jin, *Adv. Mater.*, 2014, **26**, 892-898.

19 (a) Y. W. Zhang and Z. L. Hong, *Nanoscale*, 2013, **5**, 8930-8933; (b) Y. N. Tang, W. H. Di, X. S. Zhai, R. Y. Yang and W. P. Qin, *ACS Catal.*, 2013, **3**, 405-412; (c) L. T. Su, S. K. Karuturi, J. S. Luo, L. J. Liu, X. F. Liu, J. Guo, T. C. Sum, R. R. Deng, H. J. Fan, X. G. Liu and A. L. Y. Tok, *Adv. Mater.*, 2013, **25**, 1603-1607.

20 (a) K. Prorok, A. Bednarkiewicz, B. Cichy, A. Gnach, M. Misiak, M. Sobczyk and W. Strek. *Nanoscale*, 2014, **6**, 1855-1864; (b) J. Shen, G. Y. Chen, T. Y. Ohulchanskyy, S. J. Kesseli, S. Buchholz, Z. P. Li, P. N. Prasad and G. Han, *Small*, 2013, **19**, 3213-3217.

21 H. L. Wen, H. Zhu, X. Chen, T. F. Hung, B. L. Wang, G. Y. Zhu, S. Fung Yu and F. Wang, *Angew. Chem. Int. Ed.*, 2013, **52**, 13419-13423.

22 S. Xu, W. Xu, Y. F. Wang, S. Zhang, Y. S. Zhu, L. Tao, L. Xia, P. W. Zhou and H. W. Song, *Nanoscale*, 2014, **6**, 5859-5870.

23 L. Qiang, Z. L. Cheng, G. F. Yun and L. M. Cheng, *Chin. Phys.*, 2009, **18**, 4030-4036.

24 (a) X. Li, J. Zhu and H. X. Li, *Appl. Catal., B*, 2012, **123-124**, 174-181; (b) Z. B. Wu, F. Dong, Y. Liu and H. P. Wang, *Catal. Commun.*, 2009, **11**, 82-86.

25 T. P. Cao, Y. J. Li, C. H. Wang, Z. Y. Zhang, M. Y. Zhang, C. L. Shao and Y. C. Liu, *J. Mater. Chem.*, 2011, **21**, 6922-6927.

26 (a) S. N. Habisreutinger, L. Schmidt-Mende and J. K. Stolarczyk, *Angew. Chem. Int. Ed.*, 2013, **52**, 7372–7408; (b) C. Chen, W. Ma and J. Zhao, *Chem. Soc. Rev.*, 2010, **39**, 4206-4219.

27 X. Feng, S. Zhu and H. Hou, *Environ. Technol.*, 2006, **27**, 119-126.

28 (a) E. D. Laurentiis, V. Maurino, C. Minero, D. Vione, G. Mailhot and M. Brigante, *Chemosphere*, 2013, **90**, 881-884; (b) M. V. Bosco, M. Garrido, M. S. Larrechi, *Anal. Chim. Acta*, 2006, **559**, 240-247; (c) W. Chen, P. Westerhoff, J. A. Leenheer, K. Booksh, *Environ. Sci. Technol.*, 2003, **37**: 5701-5710.

29 S. Obregón, A. Kubacka, M. Fernández-García and G. Colón, *J. Catal.*, 2013, **299**, 298-306.

30 D. Li, H. Haneda, S. Hishita and N. Ohashi, *Chem. Mater.*, 2005, **17**, 2596-2602.

31 (a) M. Liu, X. Q. Qiu, M. Miyauchi and K. Hashimoto, *Chem. Mater.*, 2011, **23**, 5282-5286; (b) T. Tachikawa, S. Yamashita and T. Majima, *J. Am. Chem. Soc.*, 2011, **133**, 7197-7204; (c) A. B. Djurišić, W. C. H. Choy, V. A. L. Roy, Y. H. Leung, C. Y. Kwong, K.W. Cheah, T. K. Gundu Rao, W. K. Chan, H. Fei Lui and C. Surya, *Adv. Funct. Mater.*, 2004, **14**, 856-864.

32 (a) F. Liao, Y. Huang, J. Ge, W. Zheng, K. Tedsree, P. Collier, X.Hong and S. C. Tsang, *Angew. Chem. Int. Ed.*, 2011, **50**, 2162–2165; (b) A. C. Papageorgiou, N. S. Beglitis, C. L. Pang, G. Teobaldi, G. Cabailh, Q. Chen, A. J. Fisher, W. A. Hofer and G. Thornton, *Proc. Natl. Acad. Sci. USA*, 2010, **107**, 2391-2396.

33 M. Setvń, U. Aschauer, P. Scheiber, Y. F. Li, W. Y. Hou, M. Schmid, A. Selloni and U. Diebold, *Science*, 2013, **341**, 988-991.